VTT Technical Research Centre of Finland

Brittle fracture initiation in decommissioned boiling water reactor pressure vessel head weld

Que, Zaiqing; Lindroos, Matti; Lydman, Jari; Hytönen, Noora; Lindqvist, Sebastian; Efsing, Pål; Nevasmaa, Pekka; Arffman, Pentti

Link to publication

Brittle fracture initiation in decommissioned boiling water reactor pressure vessel head weld

Zaiqing Que [a],*, Matti Lindroos [b],*, Jari Lydman [a], Noora Hytönen [a], Sebastian Lindqvist [a], Pål Efsing [c], Pekka Nevasmaa [a], Pentti Arffman [a]

[a] *Nuclear Reactor Materials, VTT Technical Research Centre of Finland, Espoo 02044, Finland*
[b] *Integrated Computational Materials Engineering, VTT Technical Research Centre of Finland, Tampere 33720, Finland*
[c] *Department of Solid Mechanics, Royal Institute of Technology (KTH), Stockholm SE-100 44, Sweden*

ABSTRACT

The brittle fracture initiation behavior and fracture toughness in the ductile-to-brittle transition region for a thermally-aged weld metal of a decommissioned reactor pressure vessel head (in operation at 288 °C for 23 effective full power years) and in the non-aged reference condition were investigated. The results show that brittle fracture initiated primarily from non-metallic inclusions. The correlation between fracture toughness and brittle fracture initiation type (inclusion debonding or breakage), initiator size, initiation location (as-welded or re-heated regions in the weld metal) were analysed. Despite that thermal ageing does not affect significantly the fracture toughness, it could promote the debonding as a brittle fracture primary initiation type. The influence of debonded inclusion on the evolution of cumulative damage and brittle fracture initiation was assessed using crystal plasticity modelling.

© 2022 The Author(s). Published by Elsevier B.V.
This is an open access article under the CC BY license (http://creativecommons.org/licenses/by/4.0/)

1. Introduction

The structural integrity of the reactor pressure vessel (RPV) is of utmost importance for safety and long-term operation in a nuclear power plant (NPP) [1]. During operation, the RPV is subjected to neutron irradiation and thermal aging, which can result in materials embrittlement and elevate the ductile-to-brittle transition temperature (DBTT) [2–9].

There have been extensive investigations on the weld embrittlement resulted from thermal aging and/or irradiation [10,11]. Thermal aging of a high-Ni and high-Mn weld metal (WM) in a pressurizer for 24.6 years operation at 345 °C was reported to cause an increase in DBTT [7], clustering [12] and intergranular (IG) fracture [7]. Segregation of solute elements to grain boundaries (GBs) with co-segregation process involving Cr, Ni, C, Mn, Mo and P was observed in thermally-aged RPV steel weld [13]. High bulk Ni content can encourage the formation of clusters during thermal aging, which have higher Cu and lower Ni, Mn and Si contents than the clusters found in irradiation-induced clusters [5,14,15].

In terms of embrittlement, WMs are normally considered as more critical than base materials (BM) [6], which is due to

the higher density of non-metallic inclusions and lower cohesive strength of boundaries resulted from the higher level of GB segregation in WM compared to BM [11]. WMs are typically composed of a large amount of homogeneously distributed round inclusions, which are different from the BMs where the inclusions are more irregular in shape and less densely populated. Consequently, the probability of an inclusion suitable for initiating a brittle fracture is higher in WMs than in BMs [16]. Typically, the oxygen content in arc weld metals, such as submerged arc welding (SAW) WM, can be even a magnitude higher than in BM, which favours the formation of non-metallic inclusions in WM. McMahon and Cohen [17] reported that the cracking of cementite particles located at ferrite GBs represents a primary cleavage initiation mechanism for BMs whereas non-metallic inclusions are the main cleavage initiators for WMs [18]. Hein et al. [19] had similar observations that inclusions were the primary initiators in RPV WMs. Oh et al. [20] found that the fracture toughness was inversely proportional to the square root of the triggering inclusion diameter. However, the specimens investigated were from the whole transition curve instead of basing the assessment on fracture toughness specimens from the ductile-to-brittle transition region where initiation of brittle fracture occurs after some ductile deformation. A systematic investigation on the type, location and chemical composition of the brittle fracture primary initiators in the weld metal is still pending.

---

* Corresponding authors.
  E-mail addresses: zaiqing.que@vtt.fi (Z. Que), matti.lindroos@vtt.fi (M. Lindroos).

The presence of inclusions have a significant influence on the initiation of brittle cleavage crack [21]. A microcrack of brittle fracture can initiate within a brittle particle resulted from plastic straining of the matrix surrounding the particle and propagate from the broken particle [22] or initiate at the interface between secondary particles and matrix due to debonding [23]. These modes were further referred to as inclusion cracking, inclusion-assisted cracking and inclusion decohesion by Miao and Knott [24]. A nucleated microcrack must grow to a critical size and overcome microstructural barriers such as GBs to develop into a cleavage crack with self-sustained growth subject to a high enough exterior stress beyond a sufficiently large area around the nucleation site [25]. Since a large inherent scatter is a natural part of brittle fracture, probabilistic modelling, e.g., the weakest link model is often used to describe its behavior [26,27]. However, metallurgical and microstructural data of brittle fracture initiators in real NPP component, e.g., decommissioned RPV, is required for an improved mechanistic understanding of brittle fracture.

This work aims for enhancing the comprehension of the factors affecting brittle fracture initiation by fracture toughness testing, materials characterisation and modelling of a high-Ni WM of a decommissioned boiling water reactor RPV head (RPVH). The WM is investigated in thermally-aged and reference conditions.

2. Experimental

2.1. Materials

The studied RPVH WM was harvested from the decommissioned Barsebäck Unit 2 boiling water reactor, which was in operation at 288 °C for 23 effective full power years. Barsebäck Unit 2 RPV non-irradiated non-aged state WM from the surveillance program was studied as reference material. The same type of WM has been used in several reactors [6,28]. The circumferential weld was used to join forged material (SA 508 Cl. 2) on the top and plate material (SA 533 Gr. B Cl. 1) at the lower side (Fig. 1(a)). The RPV was manufactured by Uddcomb AB, and has been post weld heat treated [29]. Trepans for tests and characterisations were drilled from the RPVH weld. The inner surface stainless steel cladding was removed before transportation of the trepans to VTT. The RPVH WM is only subjected to thermal aging but not to neutron irradiation. The investigated WM was mainly welded using SAW process with a filler material of Phoenix-Union S3NiMo with high Ni and Mn contents and low Cu content [30]. The chemical compositions of the thermally-aged RPVH WM and non-aged reference WM are presented in Table 1.

2.2. Specimens and tests

Tensile test, Charpy V-notch (CVN) impact toughness test and compact tension (C(T)) fracture toughness based T0 testing were performed. All three types of specimens were machined from a one-quarter depth from the inner surface of RPVH trepan and were fabricated in the orientation TS, which corresponds with the reference non-aged WM specimens in the Barsebäck Unit 2 surveillance program. The tensile testing with flat miniature tensile specimens was performed in accordance to ISO 6892-1 with a constant displacement rate of 0.12 mm/min at room temperature. CVN impact toughness specimens with the size of 55 mm × 10 mm × 10 mm

were tested according to the standard SFS-EN ISO-148-1:2016. Miniature C(T) specimens were manufactured from the tested CVN specimens. As shown in Fig. 1(a, b), 4 miniature C(T) specimens were manufactured from 1 CVN specimen (two from each half) and in total 20 miniature C(T) specimens from RPVH WM were manufactured and tested between −114.4 and −129.9 °C (with fracture toughness values between 51.7 and 259.8 MPa√m) for the Master curve analysis according to ASTM E1921. 11 miniature C(T) specimens of reference non-aged state were tested between −110 and −140 °C.

2.3. Materials characterisation

The metallography specimens were fine polished and etched with 3 vol% Nital solution (HNO_3 + ethanol). The weld solidification microstructure were characterised using the Zeiss Axio Observer 7 inverted light optical microscope. Reprography images were taken with Olympus OM-D E-M1 Mark II camera. Microhardness of HV1 and HV0.3 was measured using a Struers DuraScan-80 device.

A Zeiss Crossbeam 540 scanning electron microscope (SEM) equipped with EDAX Hikari Plus electron backscatter diffraction (EBSD) detector and EDAX Octane Plus Energy dispersive X-ray spectroscopy (EDS) detector was used. EBSD mapping was conducted at an accelerating voltage of 15 kV, a working distance of 14 mm and a probe current of 1.5 nA. EBSD inversed pole figure (IPF) images were analysed by TSL OIM Analysis 8 software. EDS was performed with 10−15 keV and a current density of 1.5 nA.

2.4. Modelling

A micromorphic crystal plasticity model was used to investigate the microstructural level deformation and damage behavior of the WM. Lindroos et al. described the model background in Ref. [31], in which strain gradient like micromorphic extension is used to provide scale dependent plasticity and damage behavior for martensitic steels. In the current work, micromorphic regularisation is placed on plasticity alone to control slip localisation that also affects the damage process by introducing *microslip* approach. Furthermore, previous work with micromorphic models [32,33] have been dedicated to regularise damage growth in different materials with so-called *microdamage* approach, while the objective of these models was not to apply strain gradient plasticity. Other recent approaches have focused on introducing length-scale plasticity and also its effects on ductile damage [34,35]. The present work focuses on investigating the effect of small non-metallic inclusions to the damage susceptibility within ferritic microstructures and therefore the use of scale dependent framework is supported. The following presents the key contents of the current model.

Finite strain multiplicative decomposition of the deformation gradient was employed to the elastic and inelastic contributions. Inelastic contribution considers plastic deformation by dislocation slip and damage systems. First part of this section presents the dislocation slip model and the second part focuses on the damage extension.

$$\underline{F} = \underline{F}^E \cdot \underline{F}^{IN} = \underline{E} \cdot \underline{P} \tag{1}$$

The inelastic velocity gradient is then written as:

$$\underline{P} \cdot \underline{P}^{-1} = \underline{L}^P + \underline{L}^D \tag{2}$$

Table 1
Chemical composition of studied weld metals according to optical emission spectrometry (wt.%).

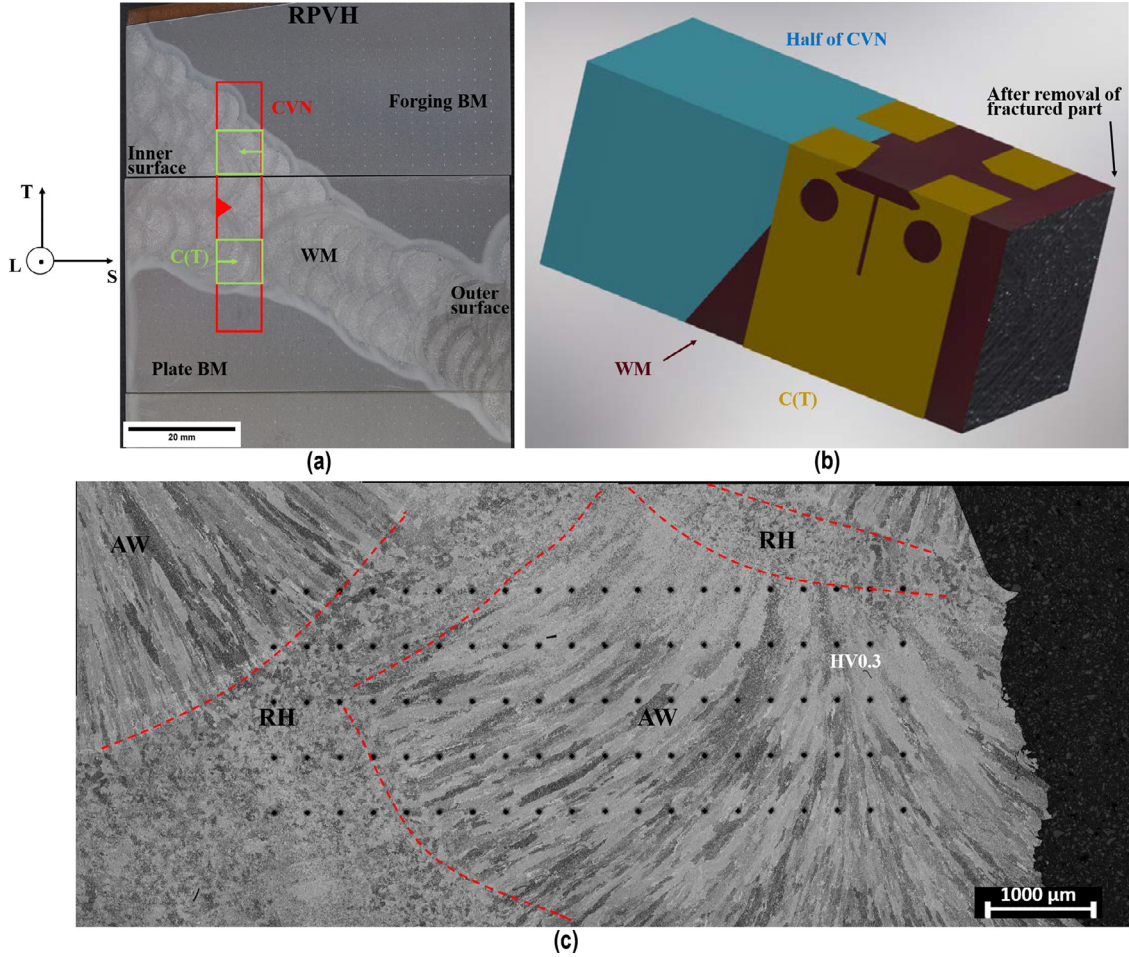| Element	C	Si	Mn	P	S	Cr	Mo	Ni	Cu	Co	Al
RPVH SAW weld	0.057	0.15	1.43	0.008	0.007	0.03	0.41	1.48	0.060	0.020	0.024
Reference weld	0.084	0.22	1.53	0.011	0.004	0.13	0.44	1.47	0.064	0.008	0.005

Fig. 1. (a) The WM was used to join the plate BM and forging BM in RPVH. The inner surface of RPVH was on the left side. (b) Two C(T) specimens were fabricated from one half of tested CVN specimen. (c) A micro-etched specimen prepared from the cross section of a tested CVN specimen showing WM microstructure includes AW and RH zones. Indentations of HV0.3 are seen as black dots.

Plastic deformation is carried over by dislocation slip. Total of 24 slip systems are included for BCC crystal, involving slip families $\{110\}{<}111{>}$ and $\{112\}{<}111{>}$ with both 12 slip systems. Plastic velocity gradient is:

$$\underline{L}^P = \sum_{s=1}^{N_s=24} \dot{\gamma}^s \underline{N}^s \tag{3}$$

where $\dot{\gamma}^s$ is the slip rate of a slip system s, and $\underline{N}^s$ is an orientation tensor. A visco-plastic slip rate is used:

$$\dot{\gamma}^s = \left\langle \frac{|\tau^s| - (R^s - S_\chi)}{K} \right\rangle^N sign(\tau^s) \tag{4}$$

where τ^s is the resolved shear stress on slip systems, R^s is the isotropic hardening of each system. K and N describe viscosity and strain rate dependency of the model. A micromorphic model extension involving a generalised stress term S_χ is introduced to accomplish length-scale dependent plasticity and therefore indirectly also a link to damage following works of Lindroos et al. [31,36]. In detail, a *microslip* variable is introduced with γ_χ as an additional degree of freedom. The model resembles a strain-gradient approach, whenever the penalisation parameters related to the micromorphic model is chosen accordingly. The effective flow rule f^s can be written using this framework by:

$$f^s = |\tau^s| - (R^s - S_\chi) = |\tau^s| - (R^s - A\, Div(Grad\,\gamma_\chi))$$
$$= |\tau^s| - (R^s - A\,\Delta_\chi \gamma_\chi)) \tag{5}$$

in which *microslip* γ_χ is related to cumulative plastic slip $\gamma_{cum} = \int_0^t \sum_{s=1}^{N_s=24} |\gamma^s| dt$ with a regularisation equation:

$$\gamma_\chi - \frac{A}{H_\chi} \Delta_\chi \gamma_\chi = \gamma_{cum} \tag{6}$$

where A is a higher order modulus and H_χ is a penalisation modulus, and Δ_χ is Lagrangian-Laplace type operator. The generalised stress term then affects slip activity and modifies a standard crystal plasticity approach.

The isotropic hardening is written as a sum of initial slip resistance τ_0 and the dislocation interaction part.

$$R^s = \tau_0 + Q \sum_{s=1}^{N_s=24} H_{rs}\{1 - \exp(-bv^r)\} + H\beta^2 v + H\beta d \tag{7}$$

where Q describes the magnitude of the hardening, H_{rs} is the interaction matrix between slip systems taken from Hoc and Forest [37], and b defines saturation of hardening. Again, the cumulative slip is tracked with $v^s = \int_0^t |\gamma^s| dt$ and the total cumulative slip v is summed over all slip systems. Total cumulative plastic slip of the slip systems is denoted by $v^{s/r}$. Coupling between plasticity and damage is performed with a parameter β and cumulative damage is denoted by d and will be defined in later section. The damage coupling terms include a self-softening term as well as a term that depends on the amount of damage coming from the free energy function suggested in Sabnis et al. [33] and Lindroos et al. [38].

A damage model is introduced with a modification to the previous works [31–33,38], where inelastic damage occurs by crystalline

cleavage planes. Cleavage planes of type [100] are considered for the present BCC material. The main inelastic deformation mechanism in the model is the opening of the [100] cleavage planes and accommodation shear mechanisms operating on the same plane. Damage rate is constructed of the opening (mode I), and shear systems (modes II and III).

$$\underline{L}^D = \sum_{a=1}^{N_{\text{damage}}} \dot{\delta}_c^a n_d^a \otimes n_d^a + \dot{\delta}_1^a n_a^a \otimes l_{d1}^a + \dot{\delta}_2^a n_2^a \otimes l_{d_2}^a \qquad (8)$$

where $\dot{\delta}_c^a, \dot{\delta}_1^a, \dot{\delta}_2^a$ are the strain rates of opening and shear systems of each damage plane, n_d^a is a normal vector to the plane and l_{d1}^a, l_{d2}^a are in-plane accommodation along shear directions. The cumulative damage strain d is computed as the sum of absolute strains generated by each opening and shear damage system.

Damage related strain rates are operated with a similar Norton type of flow rule.

$$\dot{\delta}_c^a = \left(\frac{\left| n_d^a \cdot \underline{I}^M \cdot n_d^a \right| - Y_c^a}{K_d} \right)^{N_d} sign\left(n_d^a \cdot \underline{\Pi}^M \cdot n_d^a \right) \qquad (9)$$

$$\dot{\delta}_l^a = \left(\frac{\left| n_d^a \cdot M^M \cdot l_{di}^a \right| - Y_i^a}{K_d} \right)^{N_d} sign\left(l_{di}^a \cdot \underline{\Pi}^M \cdot l_{di}^a \right), \text{ with } i = 1, 2 \qquad (10)$$

where K_d and N_d are material parameters, $\underline{\Pi}^M$ is Mandel stress in the reference configuration, and Y_c^a, Y_i^a are damage criteria. No additional micromorphic variable is placed to regularise damage growth in this work due to that the use of a single micromorphic variable for both plasticity and damage can be too restrictive [31]. The damage criteria is given as:

$$Y_c^a = Y_i^a = \sigma_d^0 + H_{soft}d + H_{soft}\beta\nu \qquad (11)$$

where σ_d^0 is the initial cleavage/damage resistance. The damage resistance is decreased by accumulation of damage. In addition, it is assumed that slip localisation makes the material more prone to damage and thus coupling with plasticity is used, whenever plastic slip accumulates. The value for the softening modulus H_{soft} is negative. A constraint is placed for both slip resistance R^s and damage resistances Y_c^a and Y_i^a to remain positive as the accumulation of damage can lead to negative values. The model is implemented to Zset finite element solver. Non-metallic aluminium oxide inclusions are included in the simulations, however, they are treated as elastic domains for simplicity with Young's modulus of 380 GPa and Poisson's ratio of 0.25.

3. Results

3.1. Baseline characterisations of thermally-aged RPVH

EBSD mappings of the RPVH WM are shown in Fig. 2. It is noteworthy to mention that the main microstructural features of the RPVH WM and the non-aged reference WM are very similar. The weld consists of as-welded (AW) and re-heated (RH) regions. In the WM, intragranular acicular ferrite with a fine basket weave structure is the dominant microstructural phase in dendritic AW region zones, as shown in Fig. 2(a). The acicular ferrite has the length of 4, 5 times of the width with ~1 to 2 μm. In addition to acicular ferrite, the AW dendrites also consist of a small fraction of pro-eutectoid GB ferrite, Widmanstätten ferrite side plates and polygonal ferrite (Fig. 2(b)). Pro-eutectoid GB ferrite appears at the dendritic boundaries.

The main microstructure of the RH zones is polygonal ferrite, as shown in Fig. 2(c, d). The prior austenite grain size in the RH

zone is ~120 μm length with 60 μm width. The polygonal ferritic microstructural boundaries is of 12 μm length with 3 μm width. Compared to the AW zones, the solidification boundaries and ferritic microstructural boundaries in RH zones tend to become more granular. No Widmanstätten ferrite side plates are present in the RH zone. Acicular ferrite is observed occasionally in RH zones. A summary of microstructures in WM is shown in Table 2.

3.2. Comparison study of thermally-aged RPVH and non-aged reference WMs

3.2.1. Mechanical properties

The comparison of mechanical properties of the decommissioned thermally-aged RPVH and non-aged reference WMs is shown in Table 3. The results of T_0 fracture toughness tests, CVN impact toughness tests and tensile tests of these two materials exhibit similar mechanical properties.

HV0.3 microhardness was measured from cross-sections of 7 and 4 CVN specimens of the decommissioned thermally-aged RPVH and non-aged reference WMs, respectively. The microhardness matrix included 100 indentations per specimen. After etching, the locations of indentations in different microstructures were identified (Fig. 1(c)). There were no significant hardness variation in the AW and RH microstructures. The summary of microhardness is presented in Table 4. The average microhardness in the WM of decommissioned thermally-aged RPVH was 214 ± 8 HV0.3 in AW and 216 ± 8 HV0.3 in RH microstructures, respectively. The average microhardness in the WM of the non-aged reference material was 209 ± 5 HV0.3 in AW and 208 ± 4 HV0.3 in RH microstructures, respectively. The mechanical test results suggest a minor (statistically insignificant) thermal embrittlement effect on the mechanical properties of the WM.

3.2.2. C(T) specimens primary initiator study

Based on ASTM E1921, the weld has a tendency to behave as a macroscopically inhomogeneous material. In this paper, though, the T_0 is estimated based on standard Master curve assessment to get an indication of the transition temperature. The T_0 temperature determined by the miniature C(T) testing of RPVH WM is −113 °C, which differs by −15 °C from the non-aged reference material condition. The brittle fracture in all the 20 miniature C(T) specimens of RPVH WM initiated from a particle with size between 0.3 and 1.8 μm. 13 out of 20 of the specimens primarily initiated from a debonded particle while the rest 7 initiated from a broken inclusion particle. Table 5 summarises the primary initiator type (as a debonded or broken particle) and the initiation location (in AW or RH microstructures). The percentage of debonded particles as primary initiating particles is higher than broken particles and there seems to be more brittle primary initiation from AW than RH regions. For the reference non-aged WM, the fractographic investigations and the determination of the primary initiation sites were performed for 11 miniature C(T) specimens. All the specimens with a determinable initiator have the brittle fracture primarily initiated from broken inclusion particles with sizes between 0.6 and 1.8 μm. As revealed by the cross-sectional metallography, 5 of the 11 primary initiation sites were found in AW microstructure and the rest in RH region.

The primary initiation site of brittle cleavage fracture can be determined based on the characteristic river patterns. For the thermally-aged RPVH WM, the fractographic examinations of two representative C(T) specimens where brittle fracture primarily initiated from a debonded particle and a broken inclusion particle are shown in Figs. 3 and 4, respectively. The specimen in Fig. 3 was tested at −128.3 °C with a fracture toughness of 81.0 MPa√m. A cross-sectional metallographic specimen right below the primary
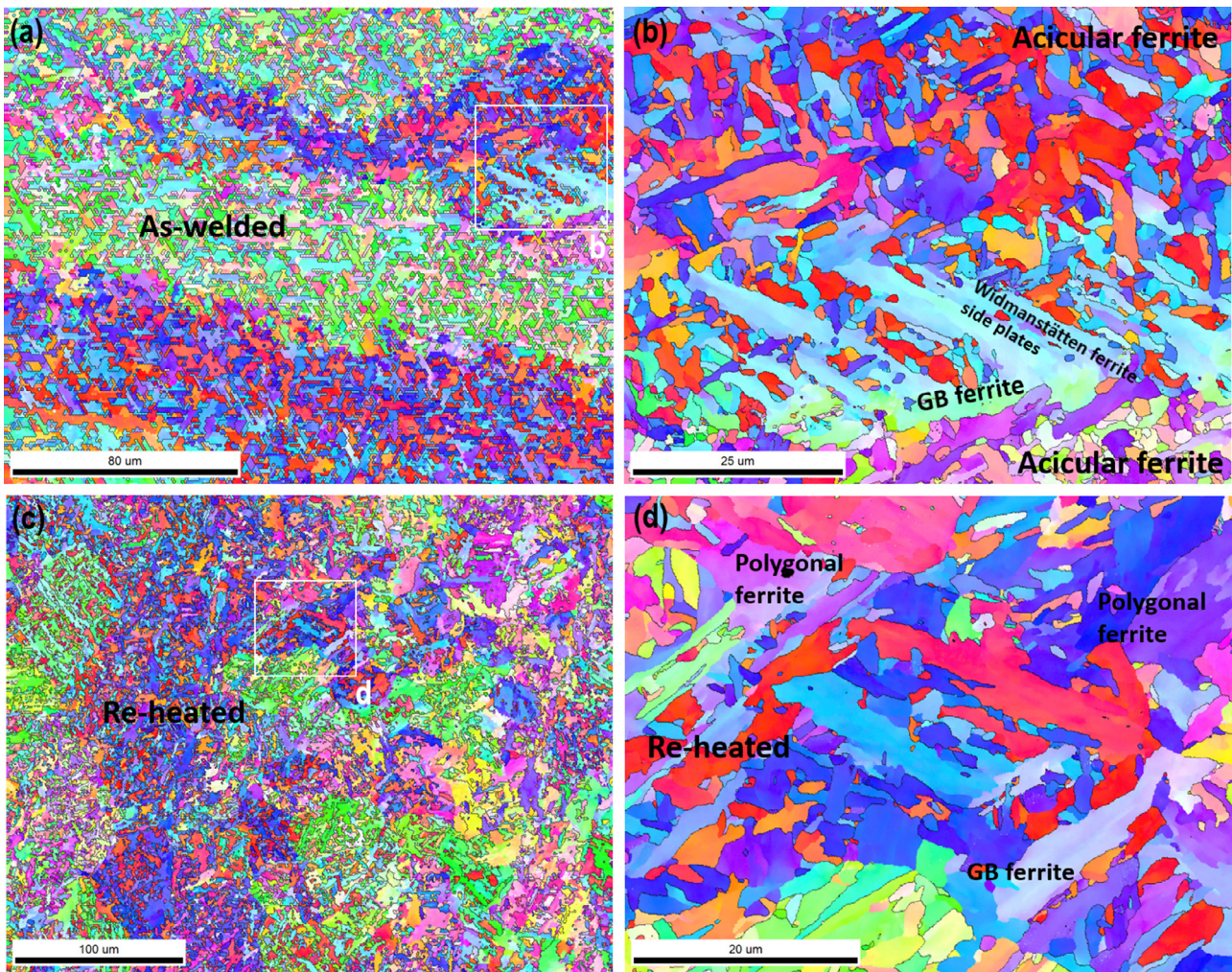
Fig. 2. EBSD mapping of (a, b) AW region and (c, d) RH region of thermally-aged RPVH material.

Table 2
Summary of grain size in various microstructures of thermally-aged RPVH material.

Microstructures	Phases or features	Grain size (μm)
As-welded	Dendritic boundary	1 mm length with 45 μm width
	Acicular ferritic GB	8−10 μm length with 1−2 μm width
Re-heated	Prior austenite GB	120 μm length with 60 μm width
	Polygonal ferritic GB	12 μm length with 3 μm width

Table 3
Mechanical properties of WMs from the decommissioned RPVH and the non-aged reference material.

Materials	Toughness		Tensile test			
	T_0 °C	T_{41J} °C	Yield stress MPa	Tensile stress MPa	Fracture strain %	Reduction of area %
Decommissioned RPVH WM	−113	−75	562.2	627.5	19.5	72
Non-aged reference WM	−98	−73	560	642	20	73.2

Table 4
Microhardness HV1 and HV0.3 of AW and RH zones from the decommissioned RPVH and the non-aged reference material.

Materials	Microstructures		HV1	HV0.3
Decommissioned RPVH	WM	AW	227 ± 5	214 ± 8
		RH		216 ± 8
Non-aged reference material	WM	AW	213 ± 3	209 ± 5
		RH		208 ± 4

initiation site was prepared by electric discharge machining as marked by the red arrow in Fig. 3(a). As shown in Fig. 3(b, c), the brittle fracture initiated from the GB ferrite in the AW microstructure. The crack growth generally follows the macroscopic microstructure of the AW dendritic boundaries and the angle between the local weld bead direction and the crack plane is ∼10°. The debonded primary initiator remained on the fracture surface of specimen half A (Fig. 3(d–f)) and on the mating fracture sur-
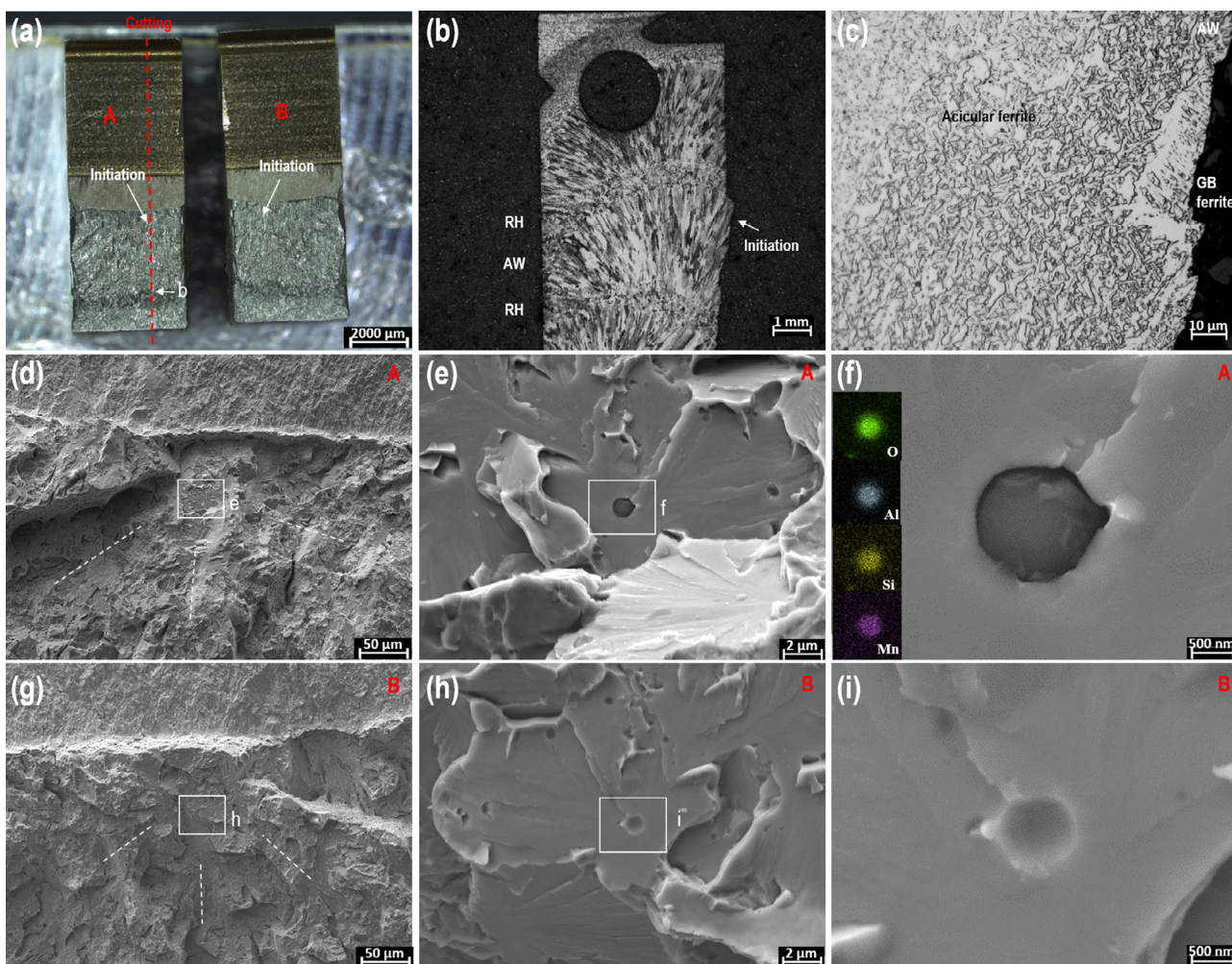
Fig. 3. (a) Parts A and B of a representative miniature C(T) specimen of the thermally-aged RPVH material (tested at −128.3 °C with fracture toughness of 81.0 MPa√m) showing the primary initiation site and the electric discharge machining cutting line. (b, c) Cross section reveals that the primary initiation locates in the AW microstructure. SEM images of primary initiation site of specimen half A (d–f) and half B (g–i). The brittle fracture initiated from a debonded inclusion.

Table 5
Summary of distribution of debonded and broken particles as the brittle fracture primary initiating particles in T0 testing C(T) specimens in AW or RH microstructures of investigated WMs.

Material	Brittle fracture primary initiation type	AW	RH
Thermally-aged RPVH WM	Debonded particle	8	5
	Broken particle	4	3
Non-aged reference material	Debonded particle	0	0
	Broken particle	5	6

face of half B there is a dent and only some traces of the particle (Fig. 3(g–i)). The primary initiation site is characterised by an Al-, Si-, Mn-rich oxide particle (with trace elements of Ti and Mg) with a size of 1.0 μm. In Fig. 4, the specimen was also tested at −128.3 °C but with a fracture toughness of 123.9 MPa√m. As shown in Fig. 4(b, c), the primary initiation site locates in the RH microstructure. The initiator particle was broken and found located in both of the specimen halves (Fig. 4(d–i)). The primary initiation site is characterised by an Al-, Si-, Mn-rich oxide particle (with trace elements of Mg, S, Ti, Cu) with a size of 1.8 μm.

The fracture surface of a representative C(T) specimens of reference non-aged material where brittle fracture primarily initiated from a broken particle is shown in Fig. 6. The specimen was tested

at −140 °C with a fracture toughness of 54 MPa√m. As shown in Fig. 6(b, c), the primary initiation site locates in the RH region with polygonal ferrite microstructure. The initiator particle was broken and found located in both of the specimen halves (Fig. 6(d–i)). The primary initiation site is characterised by a Fe-, Mn- and Mo- carbide with some traces of S. The primary initiator has an irregular shape and a size of 1.8 μm. The same irregular shape of primary initiators were found in all of specimens of reference non-aged material, which was different from the round shape of primary initiators in the RPVH specimens.

For the RPVH WM, in addition to the dominant transgranular cleavage, interdendritic (ID) and IG fracture as the secondary fracture mode is observed on the fracture surfaces in the AW and RH microstructures, respectively (Fig. 5). The representative fracture surfaces in RH region (IG and cleavage) and AW region (ID and cleavage) are shown in Fig. 5(b, c) and Fig. 5(d–f), respectively. The ID and IG fracture surface shown in Fig. 5 has propagated along the GB ferrite. The size of GB ferrite in RH microstructure is smaller than in AW microstructure (as seen in the EBSD examinations) and thus the IG fracture in RH region is more local. The size of ID and IG fracture area corresponds well with the dendrite and prior austenite grain size of AW and RH regions. The ID and IG features have been occasionally observed in the reference non-aged state WM, with the fraction being smaller than in the thermally-aged materials.
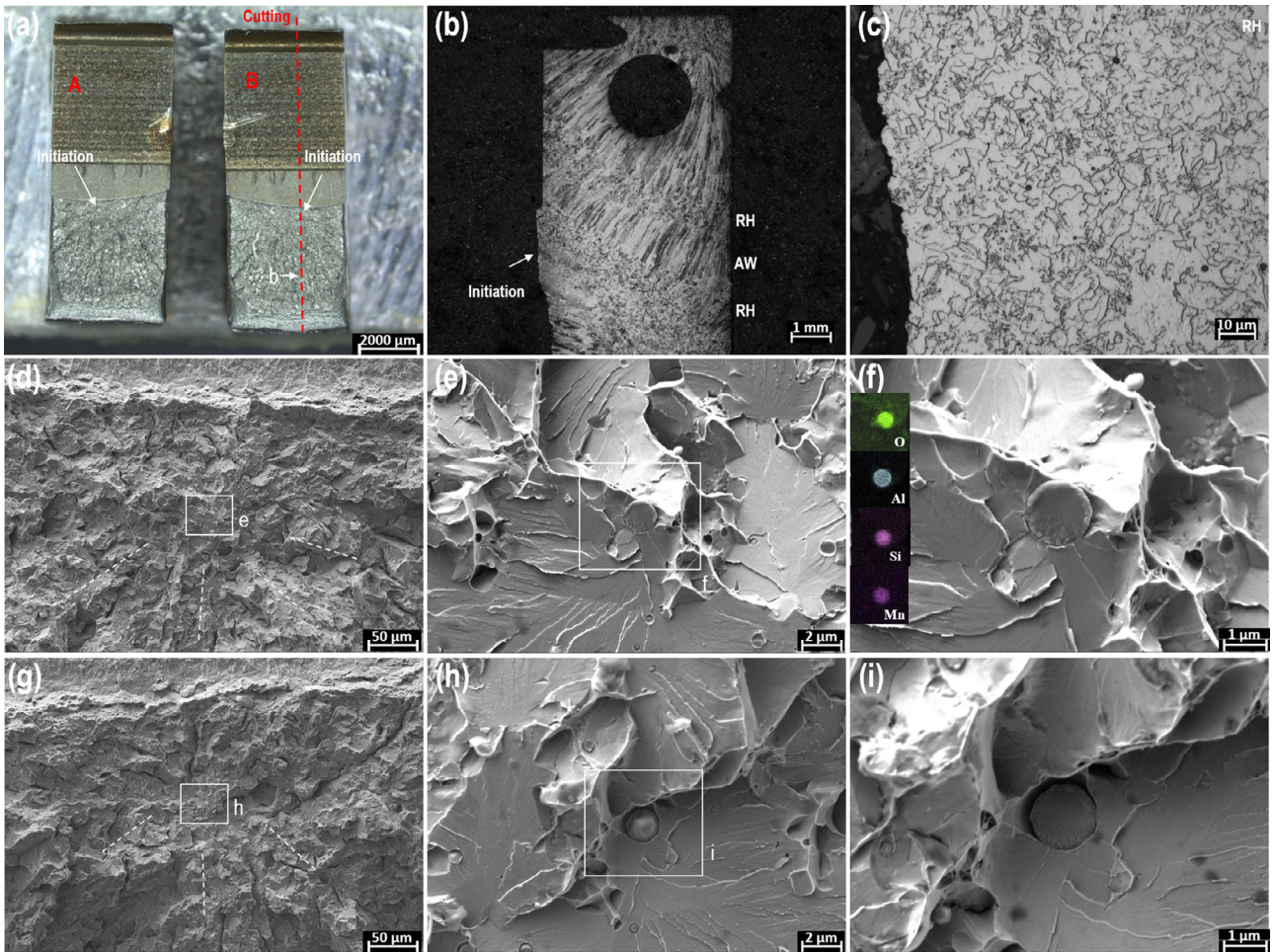
Fig. 4. (a) Parts A and B of a representative miniature C(T) specimen of the thermally-aged RPVH material (tested at −128.3 °C with fracture toughness of 123.9 MPa√m) showing the primary initiation site and the cutting line. (b, c) Cross section reveals that the primary initiation locates in the RH region. SEM images of primary initiation site of specimen half A (d–f) and half B (g–i). The brittle fracture initiated from an inclusion with breakage.
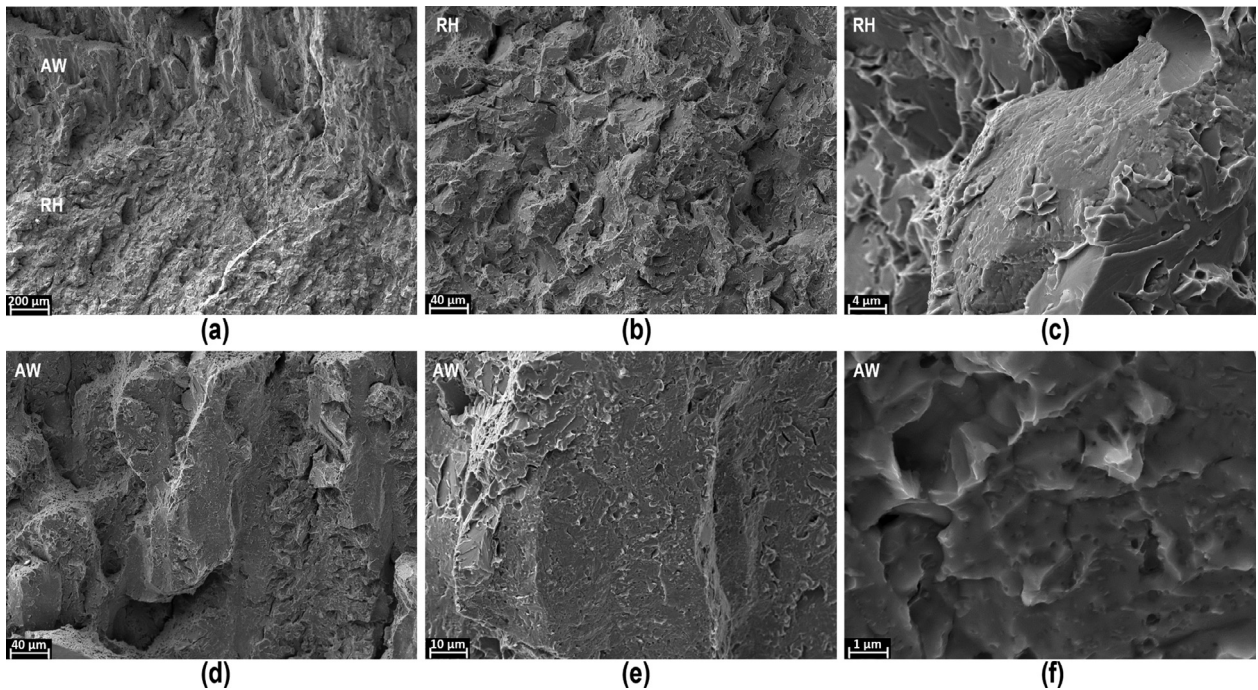
Fig. 5. (a) Representative brittle fracture surface of the thermally-aged RPVH material including both AW and RH regions. (b, c) Fracture surface of RH structure (IG and cleavage). (d–f) Fracture surface of AW structure (ID and cleavage).

Fig. 6. (a) Parts A and B of a representative miniature C(T) specimen of reference non-aged material (tested at −140 °C with fracture toughness of 54 MPa√m) showing the primary initiation site and the cutting line. (b, c) Cross section reveals that the primary initiation locates in the RH region. SEM images of primary initiation site of specimen half A (d–f) and half B (g–i). The brittle fracture initiated from an inclusion with breakage.
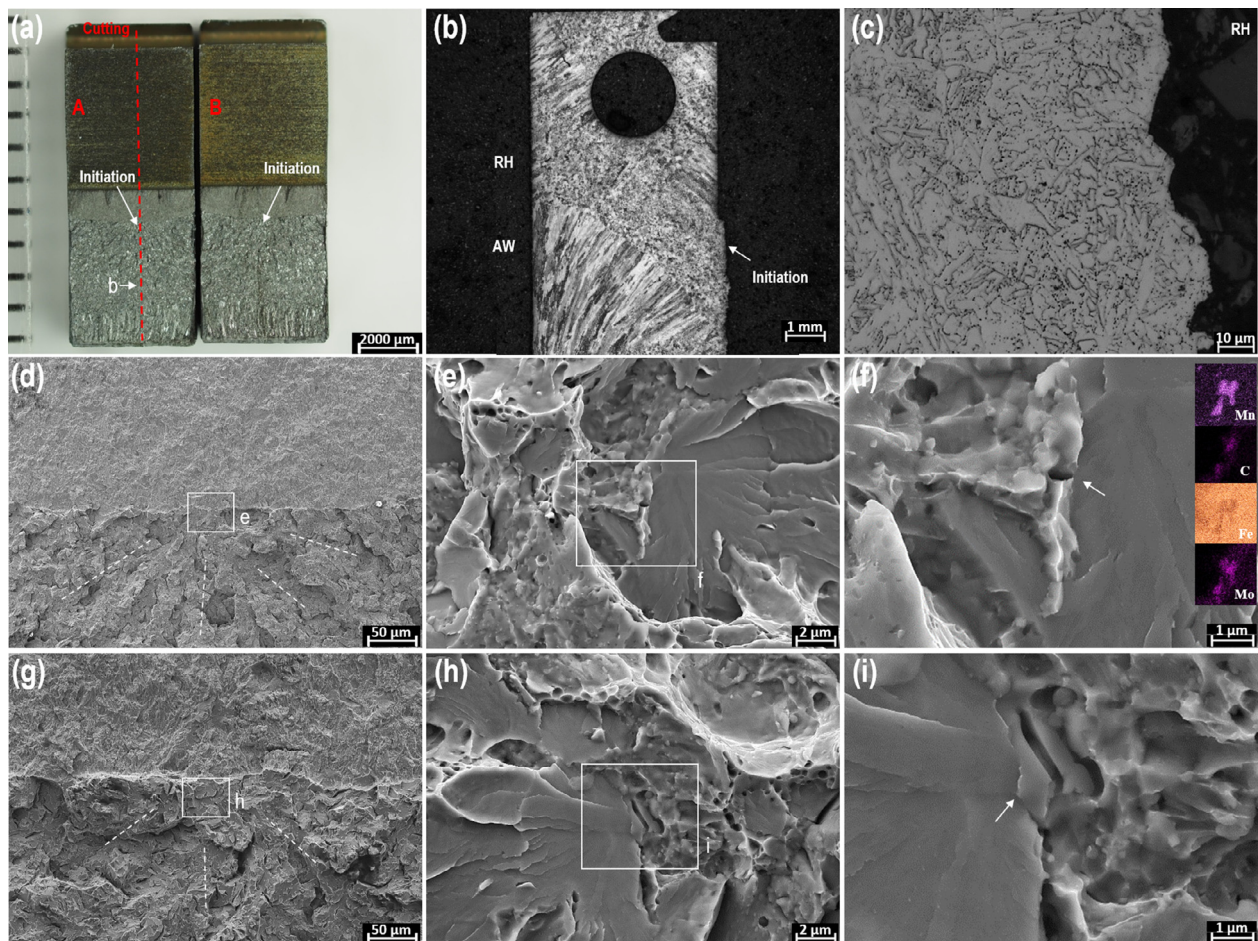
3.3. Fracture initiation modelling

3.3.1. Modelling aspects

The characteristics of the non-metallic inclusions acting as the primary initiation site for brittle failure and existing as a part of the microstructure of RPVH WM are not well known. To address some of the key features possibly leading to premature damage of the material, a non-exhaustive listing may be identified as: (i) *interface conditions between inclusion and WM matrix*, how well is the inclusions initially attached and what is the area of detachment; (ii) *multi-phase heterogeneity of the oxide-inclusion*; (iii) *prior slip localisation near the interface region from manufacturing*; and (iv) *existing pre-cracks* within the inclusions and the damage behavior of inclusions during deformation. The simulations of this work focuses on analysing the susceptibility of inclusions to cause damage in the weld microstructure. Emphasis is placed on investigating the debonding behavior of the inclusions when they are initially fully adhered to the matrix metal.

Finite element based crystal plasticity simulations were performed on EBSD-based microstructural meshes. The computational domain was constructed based on the reconstruction of grains identified by their orientation to imitate the material's microstructure utilizing a subset of the measurement data from Fig. 2(b). Tensile loading was applied to the microstructure to investigate the susceptibility for inclusions to initiate damage and to compare with experimental stress-strain curves. Kinematic uniform boundary conditions were used to retain regularity of the domain, i.e., no

localisation was allowed at the edges of the domain. Damage near the edges of the simulation domain was also prohibited to avoid interference from boundary conditions.

Three simulation cases were studied, involving a bulk microstructure without any inclusions and two microstructures containing three inclusions at different locations. The inclusion sizes range from 1.0 to 1.5 μm. No specific interface model is assigned between an inclusion and matrix and therefore any damage must occur as a description of metal failure. If the metal fails at the elements directly at the interface, it is judged as interface damage and debonding of the inclusion from the matrix, which occurs once damage resistance reaches its minimum value, i.e., crack has fully developed within the volume of the element. A transition from a nano-crack to microcrack is assumed when several elements in the cracked region are fully deteriorated and the crack itself extends significantly. Cracks can initiate anywhere in the metal matrix and they may propagate in the elements facing GB or intra-grain. GBs are modelled with an orientation change between different grains and therefore change in orientation naturally affects elastic-plastic deformation and damage responses. Table 6 lists the used crystal plasticity parameters.

3.3.2. Results from modelling

Fig. 7(a) shows the simulated and experimental strain-stress curves. Tensile strain is applied slightly exceeding the peak stress of the material to analyse the effect of inclusions on local damage. The inclusions have a slight hardening effect on the overall stress-
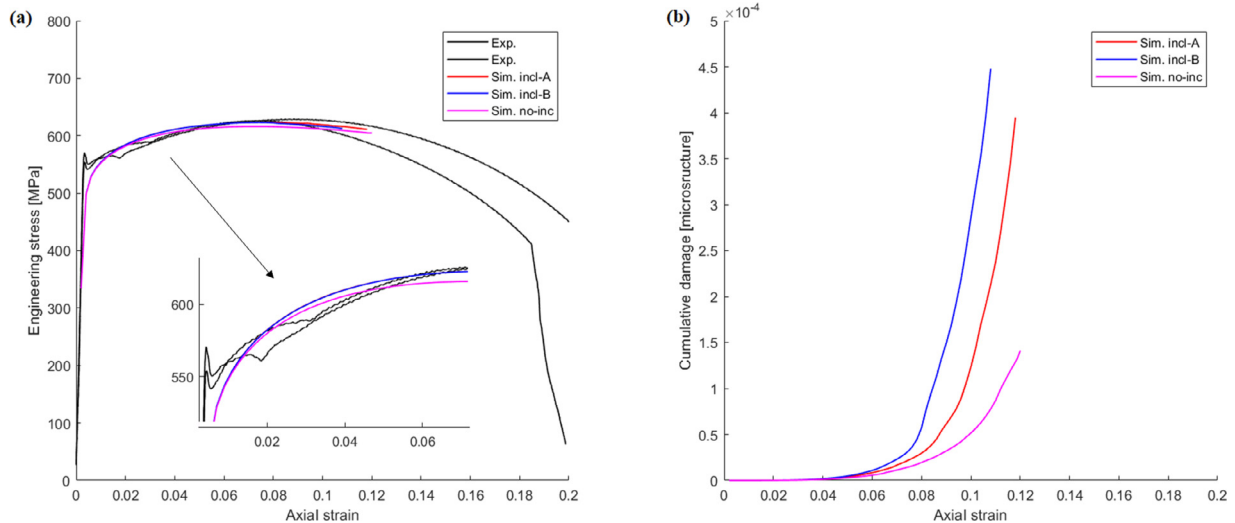
Fig. 7. (a) Experimental and simulated stress-strain curves for bulk and inclusion-containing microstructures and (b) the simulated accumulation of damage.

Table 6
Crystal plasticity parameters.

Parameter name	Parameter	Value and unit
Elastic constant	C_{11}	197 [GPa]
Elastic constant	C_{12}	134 [GPa]
Elastic constant	C_{44}	105 [GPa]
Slip parameters		
Strain rate parameter	N	15.0
Viscous parameter	K	155
Initial slip resistance	τ_0	155 [MPa]
Hardening parameter	Q	4.0 [MPa]
Hardening saturation	b	20.0
Interaction matrix	h1–h8	1.3, 1.0, 1.05, 1.15, 1.025, 1.3, 1.495, 1.0
Damage parameters		
Damage strain rate parameter	N_d	4.0
Damage viscous parameter	K_d	300.0
Initial damage resistance	σ_d^0	1300 [MPa]
Coupling plasticity-damage	β	0.25
Damage softening	H_{soft}	−3500 [MPa]
Micromorphic parameters		
Penalization modulus	H_χ	10,000.0 [MPa]
Higher order modulus	A	0.1 MPa. mm^2

strain curve in comparison to the bulk grain structure without inclusion. Fig. 7(b) shows the cumulative damage for the simulation cases. Damage initiates locally with around 5% of macroscopic strain and the presence of inclusions rapidly increases the damage rate. Fig. 8 illustrates damage maps overlain to the deformed microstructures. When there are no inclusions present, small-scale cracks emerge throughout the microstructure, especially near GBs. In both cases with inclusions, dominant cracks tend to appear primarily at the inclusion-matrix interface region and they continue to propagate to the metal matrix.

The inclusions are then partially debonded from one side or around the perimeter of the inclusion. However, it is seen in Fig. 8(c) that the inclusions do not necessarily lead to significant damage in all cases as possibly only small damage is accumulated at the vicinity of an inclusion. This indicates that the surrounding grain structure has a crucial role whenever the inclusions are judged as detrimental. The Von Mises stress contours show that inclusions affect the local stress state of the microstructure and the initiation of damage depends on the stress state and strain localisation near the inclusions, as the model couples plasticity and dam-

age. It is worth noting that the maximum damage strain is limited to 5% in the figures for clarity. However, much higher local values are observed especially near the inclusions. In this work, a fully developed crack in the material was interpreted when the local damage resistance reaches limiting value, i.e., a close to zero value but non-zero for numerical convenience.

A qualitative local analysis was performed to investigate the effects of inclusions on driving the local damage and their debonding from the matrix with more focus on mesh discretisation than larger computational domains. Fig. 9 shows the used subset of EBSD map from Fig. 2(b). Artificial inclusions are placed at a triple point (Local A) and inside a large grain (Local B) so that the edges of the inclusion appear at the GB of two neighbouring grains. Although the local microstructure contains only a small amount of grains and thus it has a limited capability to represent the whole microstructure, this local analysis provides indication of the influence of inclusion on damage. Fig. 10 shows the stress-strain curves of the three cases. Inclusions with relatively large size introduce notable additional hardening for the material, while the location of the inclusion does not show any significant effect on strain hardening. When the inclusion is placed on the triple point, Fig. 10 indicates that early damage initiation and rapid propagation is observed. The inclusion located inside a large grain in the middle of the simulation domain also promotes damage growth at the vicinity of the inclusion, further confirming that damage susceptibility of the material depends on inclusion location within the microstructure.

Fig. 11 illustrates damage growth within the microstructure and the residual Von Mises stress at specific tensile strains. Damage is mainly observed at the interface of the inclusion and matrix leading to partial separation of the inclusions. However, damage was not observed for the bulk microstructure case without inclusion in Fig. 11(a) in the current simulation, which is a result of an overall lower stress state of the local microstructure and the lack of suitable nucleation sites. It is clearly seen that the inclusions affect the local stress state and the mismatch between matrix and inclusion introduces suitable conditions for a premature failure process.

4. Discussions

4.1. Weld microstructure

The ferrite phases present in the WM of RPVH are briefly discussed as following. Acicular ferrite is the dominant phase
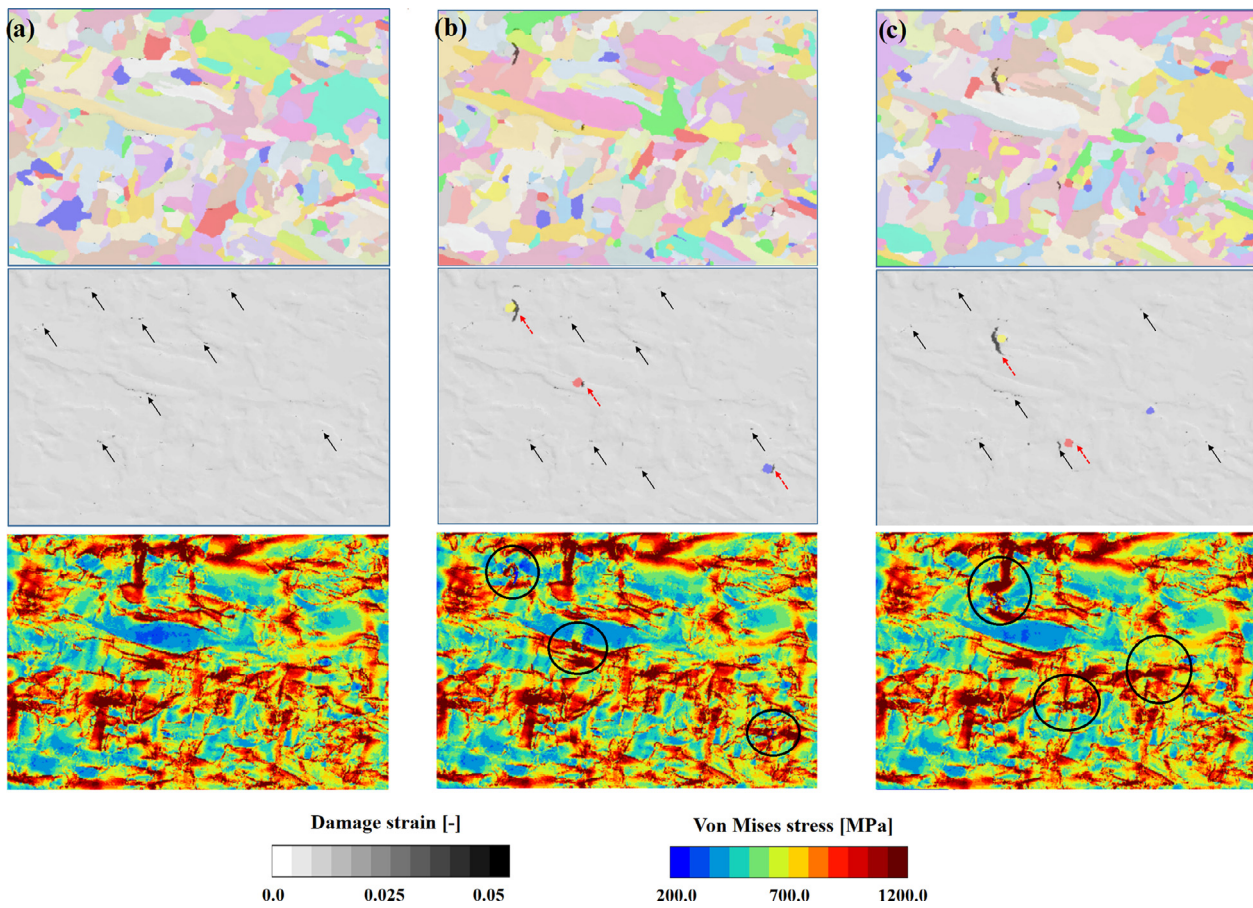
Fig. 8. Damage maps overlain to the deformed microstructure and Von Mises stress maps at the end of the simulations for (a) no inclusion, (b) case A with three inclusions, and (c) case B with three inclusions. Red arrows indicate inclusion debonding and black arrows show some of the matrix regions with initiated damage.
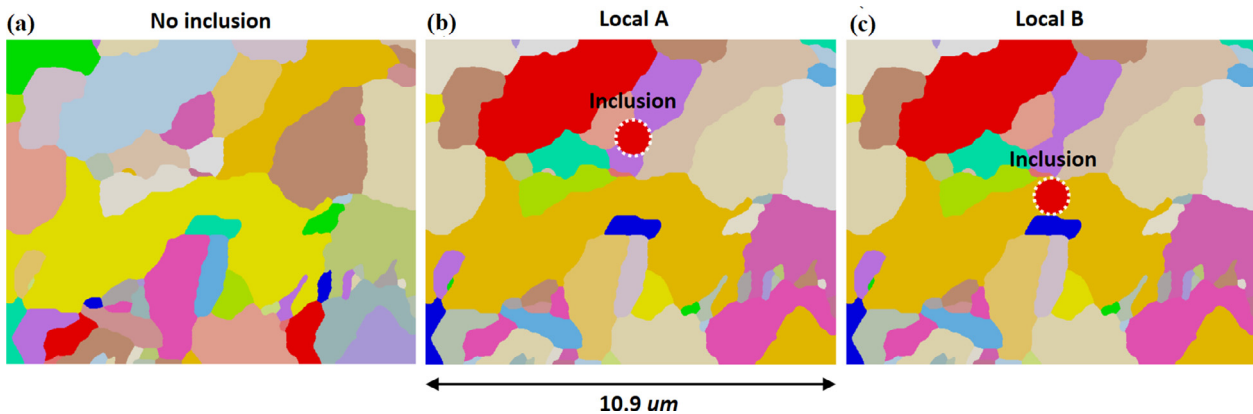

Fig. 9. Local microstructure with (a) no inclusion, (b) inclusion position A at a triple point, and (c) inclusion position B inside a grain. Size of the inclusion is circa one micron. Colours represent different grains and the inserted inclusions are highlighted.

in the AW dendrites. In addition, AW regions also consist of a small fraction of pro-eutectoid GB ferrite, Widmanstätten ferrite side plates and polygonal ferrite. Acicular ferrite is generally formed intragranularly by direct nucleation on the non-metallic inclusions, with a random crystallographic orientation and high angle boundaries between grains [39–41]. Moreover, acicular ferrites have much higher dislocation densities than GB allotriomorphic ferrite or Widmanstätten ferrite side plates [21]. These features make acicular ferrite tougher than the other ferrite phases and enable acicular ferrite laths to retard the propagation of a cleavage crack. GB allotriomorphic ferrite and Widmanstätten ferrite side plates are always present at the solidifica-

tion dendritic boundary (Fig. 2). Pro-eutectoid GB ferrite forms at austenite grain surfaces at higher temperatures during the solidification and covers the whole GBs. Widmanstätten ferrite grows along well-defined planes of the austenite and towards austenite grain interiors [42] by directly emanating from austenitic GBs or from the existing allotriomorphic GB ferrite [43–45]. Widmanstätten ferrite can be unfavourable because Widmanstätten ferrite promotes brittle crack nucleation and propagation due to that the ferrite side plates nucleate and grow as parallel plates with the same crystallographic orientation and small angle boundaries. However, only locally small amount of Widmanstätten side plate ferrite is seen in the microstructure due to a competitive na-
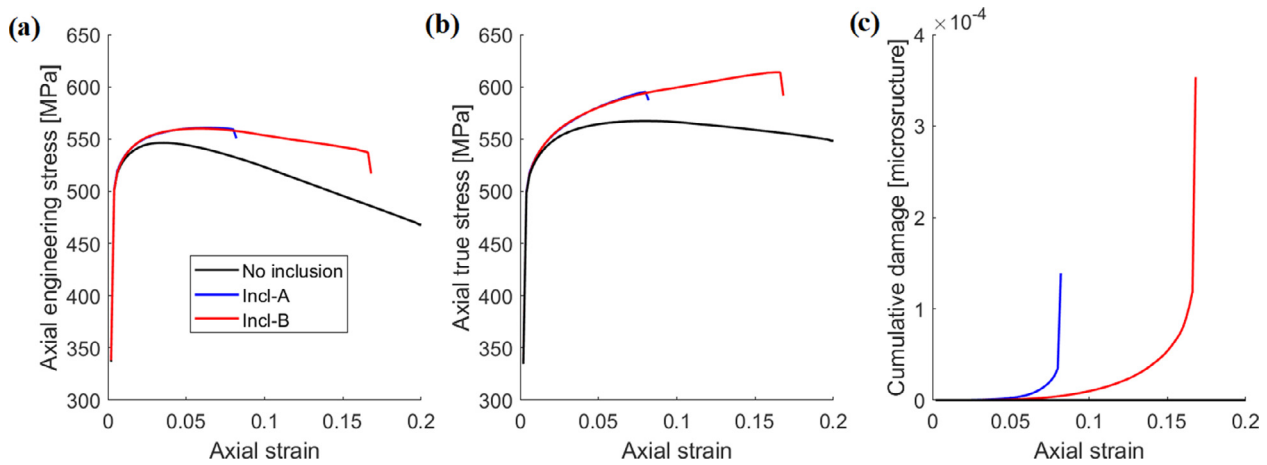
Fig. 10. (a) Engineering and (b) true stress-strain curves for a bulk material without inclusion and for the two cases with inclusions, and (c) cumulative damage strain average over the whole microstructure for the inclusions cases.
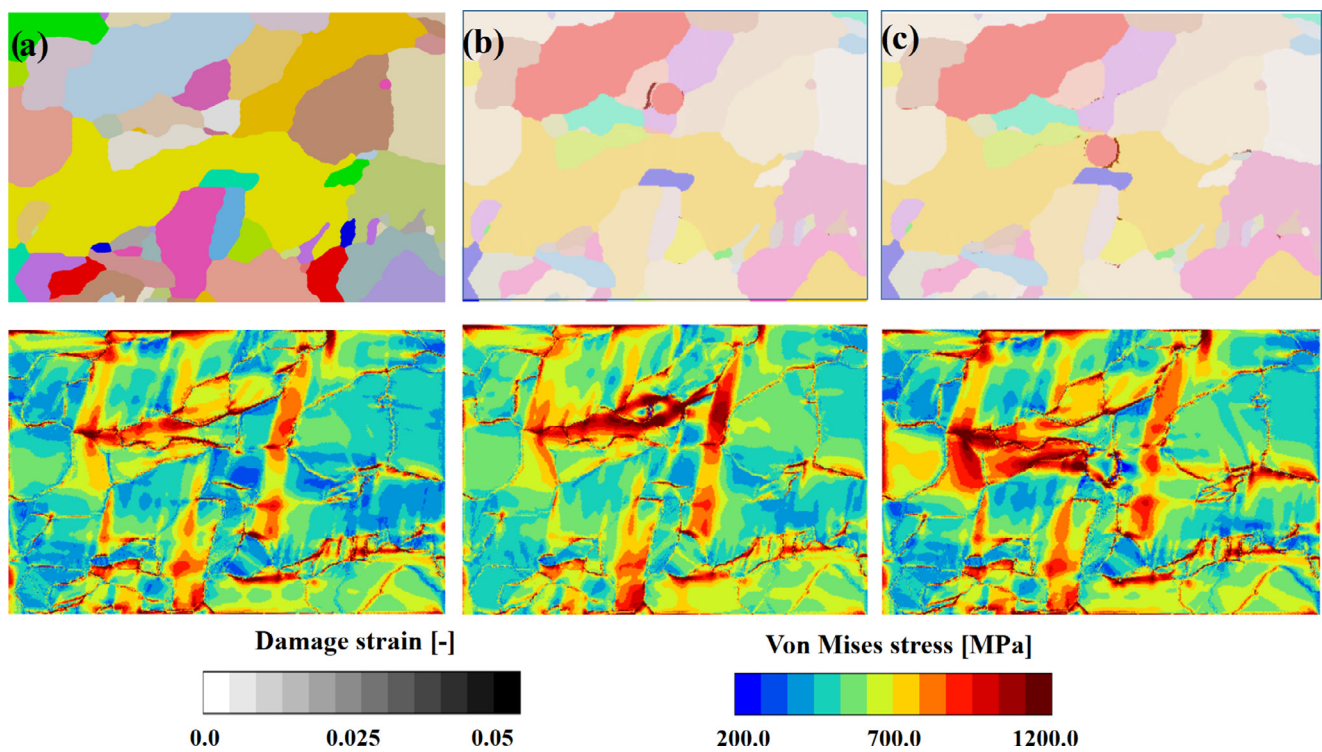

Fig. 11. Damage maps overlain to the deformed microstructure and Von Mises stress contours for (a) the local bulk material without inclusion at 16.8% of strain, (b) inclusion case A at 8.2% of strain, and (c) inclusion case B at 16.8% of strain. Tensile direction is from left to right.

ture between the formation of acicular ferrite and Widmanstätten side-plate ferrite, thus it did not play a major role in this study.

The RH zone is formed when the weld bead receives heat input again when welding a new weld bead on its top. Therefore, the RH zone is mainly consisted of polygonal ferrite due to the grain reconstruction and carbon diffusion with the new heat input. Compared to the AW zone, solidification boundaries and intragranular polygonal microstructural boundaries in RH zone also tend to become more granular. No Widmanstätten ferrite side plates are present in the RH zone.

The toughness of the WM mainly depend on the microstructure and proportion of different ferrite phases [46], particularly by the acicular ferrite. The AW microstructure is in general tougher than the RH region. The toughness decreases with an increasing amount of GB ferrite structure. The ID and IG fracture observed

in this work confirm the weakening role of GB ferrite. ID fracture was observed in the AW region in C(T) specimens where the angle between the cracking plane and dendrite structure is low, i.e., < 25°. When the angle between brittle fracture cracking and dendrite structure is high, i.e., > 45°, no ID feature was found on the fracture surface. Therefore, a low angle between the pre-fatigue crack plane and the local dendrite orientation in the weld bead structure can be a prerequisite for ID cracking. If the angle is high, the brittle fracture propagates through the grains and results in cleavage fracture.

4.2. Correlation between toughness and brittle fracture initiation site

The critical local normal stress for non-metallic inclusion is generally lower than for structural boundaries/barriers at equal fracture toughness level [11], which results in the energy-
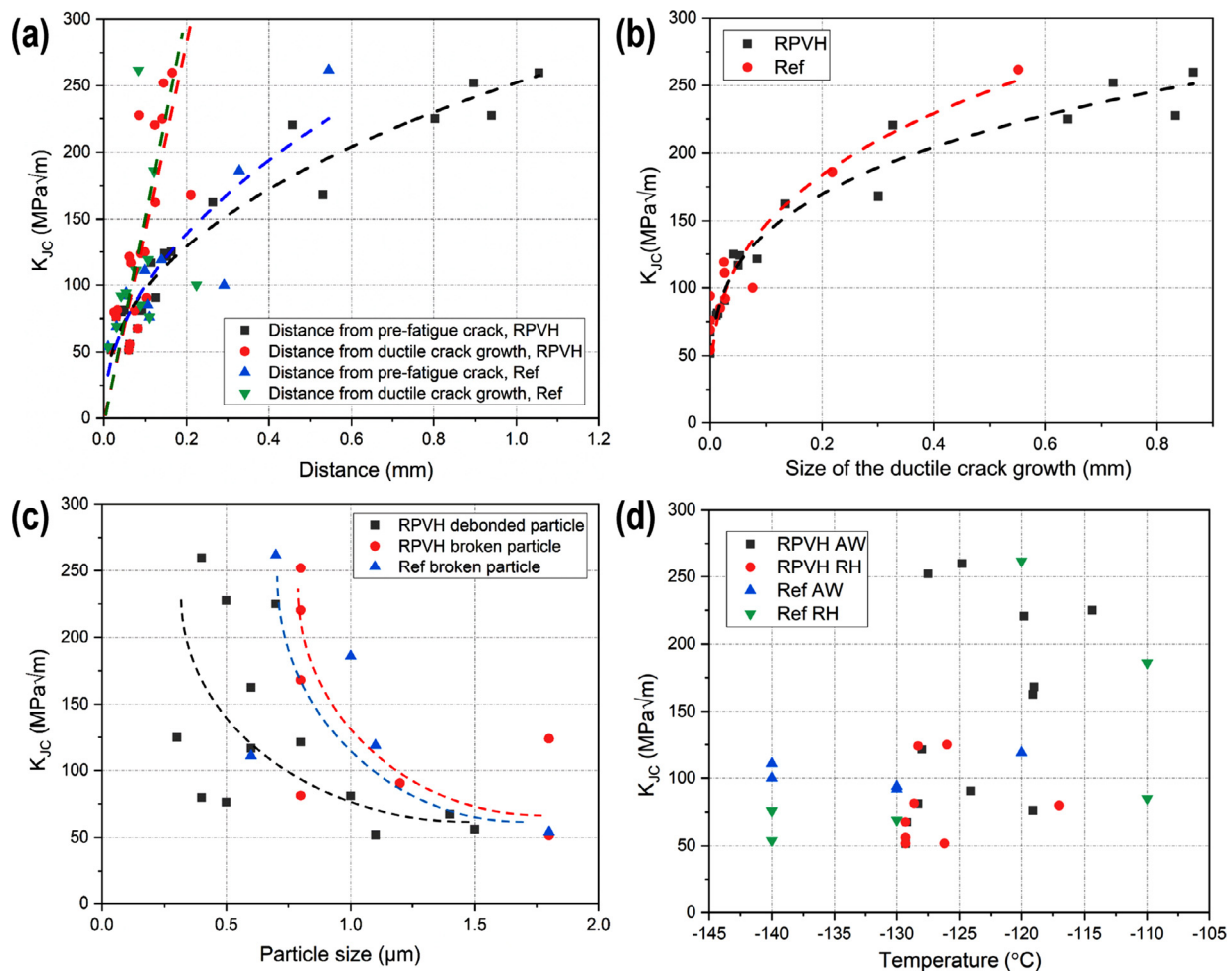
Fig. 12. Fracture toughness tests summary of the thermally-aged RPVH material and the reference non-aged WM. (a) Fracture toughness vs the distances of initiation sites from end of pre-fatigue (black square) and end of ductile crack growth (red circle). (b) Fracture toughness vs size of the ductile crack growth prior to brittle fracture. (c) Fracture toughness vs the initiating particle size (including both debonded and broken primary initiation particles). (d) Fracture toughness vs testing temperature and initiating microstructures.

preferable brittle fracture initiation from non-metallic inclusions. As revealed in this work, all brittle fracture primary initiation sites are non-metallic inclusions. For the thermally-aged RPVH WM, the majority of the primary initiators (with sizes of 0.3−1.8 μm) in T_0 testing specimens are debonded particles. For the reference non-aged WM, only broken inclusion particles with size of 0.6−1.8 μm were found in the T_0 testing C(T) specimens.

Some observations revealed by T_0 testing of thermally-aged RPVH material and the reference non-aged WMs are summarised in Fig. 12:

- The distance of primary initiation site from pre-fatigue crack front shows a correlation to the fracture toughness, Fig. 12(a). Specimens with higher fracture toughness values have initiation sites further from the pre-fatigue crack tip than specimens with lower fracture toughness. This follows the theory of weakest link, as there are initially no critical locations in the process zone close to the crack, the load increases together with the fracture process zone until a critical location is reached. The correlation follows a power law fitting.
- Though the C(T) specimens were tested at low temperatures and have a dominant brittle fracture, some small extents of preceding plastic deformation and ductile fracture prior to the brittle fracture were observed. A linear relation between the fracture toughness and the distance of initiator from the end of prior ductile crack growth is obtained (Fig. 12(a)). The two

types of fitting curves in Fig. 12(a) shows elastic plastic and linear elastic behavior, respectively.
- Specimens with higher fracture toughness values have more prior ductile crack growth. The size of the ductile crack growth ranged from ∼0 to 0.865 mm. Fig. 12(b) shows a power law behavior and the fitting line for thermally-aged RPVH material seems to be slightly lower than that of the reference non-aged WM. Local plasticity at boundaries of inclusions are required to initiate cleavage fracture [47].
- Lower fracture toughness values are obtained in specimens with larger initiating particle size, as shown in Fig. 12(c). The required applied global stress for causing final fracture can be lower for larger particles since a larger particle creates a larger initial microcrack with higher energy release rate for easier crack propagation to the matrix. Similar observations were reported in literature [11,47].
- Brittle fracture of 13/20 of the C(T) specimens of RPVH WM initiated from a debonded particle while 7/20 initiated from broken particles. All of the initiating particles with a size < 0.7 μm are debonded type and the initiators with a size of >1.6 μm are broken. Primary initiation particles between 0.7 and 1.6 μm are either broken or debonded. As shown in Fig. 12(c), with a similar initiator particle size, specimens with debonded initiators are likely to have a lower fracture toughness than the specimens with broken inclusions. Due to the large scatter in the

data points, an absolute conclusion requires more data. The fitted curves of the broken initiators of RPVH WM and reference non-aged WM in Fig. 12(c) are close to each other.

- Fig. 12(d) shows the fracture toughness as a function of test temperature and initiating microstructure (i.e., AW or RH regions). Specimens, in which brittle fracture initiated in the RH microstructure have lower fracture toughness values compared to specimens with initiation from the AW microstructure, particularly for thermally-aged RPVH material. The T_0 is -113 °C and -85 °C for the AW and RH structures in the RPVH material, respectively. As discussed in Chapter 4.1, the toughness of the acicular ferrite (the major microstructure in AW region) was higher than the other ferritic microstructure.

4.3. Brittle fracture initiation

In this work, a brittle fracture microcrack initiates either within the multi-phase oxide inclusions (leading to initiator breakage) or from the debonded interfaces between the uncracked inclusions and WM matrix (resulting into debonded initiator). The average diameter of inclusions in the investigated RPVH WM is ≤ 0.3 µm [30]. According to the weakest link theory, the brittle fracture initiates within the effective process zone from the weakest location (biggest inclusion). Based on the semi-quantitative EDS mapping from the primary brittle fracture initiation sites in RPVH WM, the initiators are generally multi-phase oxides with main elements of Mn, Si, and Al and other trace elements like S, Mg and Cu, which is similar to that found in thermally-aged WM in literature [20]. Depending on the particle size, chemical composition and surface status of the inclusions, stress state and testing temperature, the brittle microcrack initiates either by debonding or breakage in WM of thermally-aged RPVH. The oxides or carbides with a more brittle nature fulfil the Griffith criterion of brittle fracture initiation. With the existing defects or inclusion boundaries, the microcrack initiates within the inclusion, results in the breakage of the inclusion and further induces cleavage fracture [23]. For oxysulfides that are more ductile, void nucleation and coalescence at the particle-matrix interface result in debonding of the interfaces of intact inclusions to WM matrix. The exterior stress, which exceeds critical local normal stress [11], breaks the interatomic bonding between the inclusion and the matrix. Moreover, irregular-shape carbide type and round-shape oxide type initiators were found in specimens of reference non-aged and the RPVH specimens, respectively. The reason for the change of shape of the brittle fracture primary initiators is unclear. Nevertheless, irregular inclusions have sharp corners for high stress concentration, which might assist in the inclusion breakage.

For the decommissioned thermally-aged RPVH, there are more debonded initiators than broken initiators in T_0 testing specimens. However, WM of the non-aged reference condition revealed dominant broken primary initiators in T_0 testing specimens. It indicates that thermal aging could promote debonding as the brittle fracture initiation mechanism. Though macroscopically the thermal embrittlement effect on toughness are not significant (due to the moderate thermal aging temperature, low matrix P content and possibly also the absence of neutron irradiation in RPVH WM), the thermal aging could promote the interface/boundary segregation and thus debonding phenomenon [48,49]. The long-term thermal operation can enhance the elemental segregation of impurities (e.g., P, S, etc.) to the particle surfaces and GBs and decrease the cohesion strength of the particle-matrix interface [11]. The high nickel content of the WM can accelerate the process of P segregation [9]. Miao and Knott [24] reported that fracture toughness was not significantly changed with the formation of sulphide coatings on the surface of inclusions but the primary

initiation from debonded particles were clearly associated with sulphide "patches" on inclusions. In the study by Boåsen et al. [25] [50], enhanced debonding as a consequence of thermal aging was reported. Filho et al. [47] reported the fracture stresses produced by failure from cracked inclusions are not significantly different to that produced when inclusions were decohered from matrix. This means that as inclusion cracks, it partly blunts out at the interface and thus leads to a similar level of fracture stress that is not much higher than from a decohered inclusion. This is in line with the finding in Fig. 12(c) and it further indicates the potential role of thermal aging in promoting the brittle fracture initiation with decohesion/debonding and the fracture stresses required are not fundamentally different.

4.4. Correlation of brittle fracture with crystal plasticity modelling

Though the C(T) specimens were tested at low temperatures and have a dominant brittle fracture failure, preceding plastic deformation and ductile fracture prior to brittle fracture are required and were observed on the fracture surface. Local plasticity at boundaries between inclusions and WM matrix are required to initiate the cleavage fracture. Crystal plasticity simulations were performed to investigate the effect of debonding non-metallic oxide inclusions on damage initiation. The grain structure imposes heterogeneous stress fields under deformation with typical interactions between the grains and elevated stress concentrations near GBs, as was shown in Figs. 8(a) and 11(a). The simulations performed on microstructures containing oxide inclusions show that the local stress state of the material is altered. If the inclusions are fully attached to the matrix, it tends to temporarily strengthen the microstructure, while in turn providing more convenient conditions for damage to occur depending on the orientations and morphology of the surrounding grains. The crystal plasticity simulations effectively show the debonding of the inclusions as a premature damage mechanism.

However, inclusion breakage was not treated with the model in the absence of damage model assigned to the inclusions themselves and thus no separation between debonding and particle breakage promoted cracking was done. Yet, once the interface has effectively separated, the crack front can continue to propagate in the matrix grains quickly after debonding had taken place, while some cracks remained arrested at the matrix GBs. This behavior describes the semi-brittle behavior of the material, where further deformation could allow significant and fatal crack growth. It was also noted that not all inclusions promote inclusion debonding from the matrix, as they can also support matrix damage process away from the interface due to the alterations in the local stress and strain fields, as is seen in Fig. 8(c).

The simulations were restricted to 2D EBSD map based grain structures, which enforces planar stress-strain states and damage growth. This limits the prediction capability of the modelling approach to further investigate large growth of damage in the material as crack growth process is essentially a 3D process, and therefore simulations were restricted to early damage phenomena. Future research could be focused on preparing sufficiently representative 3D microstructures and to have sensitivity analysis on various types of inclusions in the material as well as involvement of fracturing inclusions. Furthermore, the inclusion-matrix interface conditions are not necessarily ideal as the inclusions can be weakly adhered to the matrix or partially separated. The inclusions themselves may be heterogeneous that could be significant in terms of the overall local failure process (debonding/inclusion breakage). Such efforts require well-described synthetic and realistic 3D grain structure, either by serial-slicing EBSD reconstruction or volume-scanning synchrotron measurement.

5. Conclusions

In this work, the initiation of brittle fracture in thermally-aged high-Ni WM from a decommissioned BWR RPVH (in operation at 288 °C for 23 effective full power years) was investigated and compared to its non-aged reference condition. The mechanical testing, microstructure characterisation, fractographic examination and modelling revealed the following conclusions:

- The influence of long-term thermal aging on the fracture and impact toughness, hardness, and tensile properties of the WM in decommissioned thermally-aged RPVH compared to the non-aged reference condition are not significant.
- In the RPVH WM, round-shape oxide type initiators are found at the primary initiation sites for brittle failure and there are more debonded inclusion than broken inclusions. For the reference non-aged WM, irregular-shape and broken carbide type of primary initiators are found.
- Thermal aging could promote the debonding at the brittle fracture primary initiation sites possibly due to enhanced segregation. The long-term thermal operation promote the elemental segregation of impurities (e.g., P, S, etc.) to the particle surfaces and GBs and decrease the cohesion strength of the particle-matrix interface or GBs and facilitate the occurrence of cleavage fracture event.
- Transgranular cleavage as the dominant fracture mechanism and ID and IG fracture as the secondary fracture mode are observed. The amount of IG fracture appears to be higher in the RPVH samples than the reference material.
- Fracture toughness increases with the distance of the initiation site from the pre-fatigue crack and the size of the prior ductile crack growth before brittle fracture initiation, but decreases with the size of the initiator particle. Specimens with debonded initiators are likely to have a slightly lower fracture toughness than the specimens with broken inclusions with a similar size of primary initiator. Specimens, in which brittle fracture initiates in the RH microstructure have lower fracture toughness values compared to specimens, where initiation occurs in the AW microstructure.
- The crystal plasticity modelling with a semi-brittle behavior of the WM microstructure (EBSD-based microstructural meshes) exhibiting plasticity prior to fracture, revealed the promoting role of debonded inclusions for the premature evolution of cumulative damage and cleavage cracking. Damage is mainly observed at the interface of the inclusion and matrix leading to partial separation of the inclusions and the microcrack that forms continue to propagate to the metal matrix. And the severity of damage caused by inclusions depend on the location of the inclusion, surrounding matrix and grain orientation.

Declaration of Competing Interest

The authors declare that they have no known competing financial interests or personal relationships that could have appeared to influence the work reported in this paper.

CRediT authorship contribution statement

Zaiqing Que: Conceptualization, Data curation, Formal analysis, Investigation, Methodology, Supervision, Writing – original draft, Writing – review & editing. **Matti Lindroos:** Conceptualization, Data curation, Formal analysis, Investigation, Methodology, Writing – original draft. **Jari Lydman:** Conceptualization, Data curation, Formal analysis, Investigation, Methodology, Writing – review & editing. **Noora Hytönen:** Data curation, Formal analysis, Investigation, Writing – review & editing. **Sebastian Lindqvist:** Investigation, Methodology, Writing – review & editing. **Pål Efsing:** Conceptualization, Project administration, Resources, Supervision, Writing – review & editing. **Pekka Nevasmaa:** Conceptualization, Writing – review & editing. **Pentti Arffman:** Conceptualization, Funding acquisition, Data curation, Project administration, Resources, Writing – review & editing.

Data availability

Data will be made available on request.

Acknowledgments

References

[1] W. Morgan, J. Livingston, A Review of Information for Managing Aging in Nuclear Power Plants, Pacific Northwest Laboratory, 1995.

[2] P. Haušild, C. Berdin, P. Bompard, Prediction of cleavage fracture for a low-alloy steel in the ductile-to-brittle transition temperature range, Mater. Sci. Eng. A 391 (1–2) (2005) 188–197.

[3] Y. Shtrombakh, B. Gurovich, E. Kuleshova, D. Maltsev, S. Fedotova, A. Chernobaeva, Thermal ageing mechanisms of VVER-1000 reactor pressure vessel steels, J. Nucl. Mater. 452 (2014) 348–358.

[4] IAEAIntegrity of Reactor Pressure Vessels in Nuclear Power Plants: Assessment of Irradiation Embrittlement Effects in Reactor Pressure Vessel Steels, International Atomic Energy Agency Nuclear Energy, 2009 Series No. NP-T-3.11.

[5] J. Hyde, G. Sha, E. Marquis, A. Morley, K. Wilford, T. Williams, A comparison of the structure of solute clusters formed during thermal ageing and irradiation, Ultramicroscopy 111 (2011) 664–671.

[6] K. Lindgren, M. Boåsen, K. Stiller, P. Efsing, M. Thuvander, Evolution of precipitation in reactor pressure vessel steel welds under neutron irradiation, J. Nucl. Mater. 488 (2017) 222.

[7] P. Joly, L. Sun, P. Efsing, J. Massoud, F. Somville, R. Gerard, Y. An, J. Bailey, Characterization of in-service thermal ageing effects in base materials and welds of the pressure vessel of a decommissioned PWR pressurizer, after 27 years of operation, in: Proceedings of the 19th International Conference on Environmental Degradation of Materials in Nuclear Power Systems-Water Reactors 2019, Boston, 2019.

[8] D. Sprouster, J. Sinsheimer, E. Dooryhee, S. Ghose, P. Wells, T. Stan, N. Almirall, G. Odette, L. Ecker, Structural characterization of nanoscale intermetallic precipitates in highly neutron irradiated reactor pressure vessel steels, Scr. Mater. 113 (2016) 18.

[9] B. Margolin, E. Yurchenko, A. Morozov, D. Chistyakov, Prediction of the effects of thermal ageing on the embrittlement of reactor pressure vessel steels, J. Nucl. Mater. 44 (2014) 107–114.

[10] B. Gurovich, A. Chernobaeva, D. Erak, E. Kuleshova, D. Zhurko, V. Papina, M. Skundin, D. Maltsev, Chemical composition effect on VVER-1000 RPV weld metal thermal aging, J. Nucl. Mater. 465 (2014) 540–549.

[11] E. Kuleshova, A. Erak, A. Kiselev, S. Bubyakin, A. Bandura, Influence of operation factors on brittle fracture initiation and critical local normal stress in SE(B) type specimens of VVER reactor pressure vessel steels, J. Nucl. Mater. 467 (2015) 927–936.

[12] K. Lindgren, M. Boåsen, K. Stiller, P. Efsing, M. Thuvander, Cluster formation in in-service thermally aged pressurizer welds, J. Nucl. Mater. 504 (2018) 23.

[13] P. Styman, J. Hyde, K. Wilford, A. Morley, G. Smith, Precipitation in long term thermally aged high copper, high nickel model, Prog. Nucl. Energy 57 (2012) 86–92.

[14] P. Styman, J. Hyde, A. Morley, K. Wilford, N. Riddle, G. Smith, The effect of Ni on the microstructural evolution of high Cu reactor pressure vessel steel welds after thermal ageing for up to 100,000 h, Mater. Sci. Eng. A 736 (2018) 111–119.

[15] K. Lindgren, M. Boåsen, Z. Que, K. Stiller, P. Efsing, M. Thuvander, Post-irradiation annealing of high flux irradiated and surveillance material reactor pressure vessel weld metal, J. Nucl. Mater. 562 (2022) 153586.

[16] P. Bowen, S. Druce, J. Knott, Effects of microstructure on cleavage fracture in pressure vessel steel, Acta Metall. 34 (6) (1986) 1121.

[17] C. McMahon, M. Cohen, Initiation of cleavage in polycrystalline iron, Acta Metall. 13 (6) (1965) 591–604.

[18] D. Fairchild, D. Howden, W. Clark, The mechanism of brittle fracture in a microalloyed steel: part I. inclusion-induced cleavage, Metall. Mater. Trans. A 31A (2000) 641–652.

[19] H. Hein, J. Kobiela, M. Brumovsky, C. Huotilainen, J. Lydman, B. Marini, B. Radiguet, O. Startsev, M. Serrano Garcia, R. Hernandez Pascual, F. Roeder, H. Viehrig, Addressing of specific uncertainties in the determination of RPV fracture toughness in the SOTERIA project, in: Proceedings of the Fontevraud 9-Contribution of Materials Investigations and Operating Experience to Light Water NPPs' Safety, Performance and Reliability, Avignon, 2018.

[20] Y. Oh, B. Lee, J. Hong, The effect of non-metallic inclusions on the fracture toughness master curve in high copper reactor pressure vessel welds, J. Nucl. Mater. 301 (2002) 108–117.

[21] D. Sarma, A. Karasev, P. Jönsson, On the role of non-metallic inclusions in the nucleation of acicular ferrite in steels, ISIJ Int. 49 (7) (2009) 1063.

[22] A. Griffith, The phenomena of rupture and flow in solids, Philos. Trans. R. Soc. Lond. 221 (1921) 163.

[23] A. Pineau, A. Benzerga, T. Pardoen, Failure of metals I: Brittle and ductile fracture, Acta Mater. 107 (2016) 424.

[24] P. Miao, J. Knott, Effects of Inclusions and their surface chemistry on cleavage fracture in a C-Mn steel weld metal, in HSLA Steels 2015, Microalloying 2015 & Offshore Engineering Steels 2015, Springer, 2015.

[25] M. Boåsen, C. Dahlberg, P. Efsing, J. Faleskog, A weakest link model for multiple mechanism brittle fracture-model development and application, J. Mech. Phys. Solids 147 (2021) 104224.

[26] W. Weibull, A statistical distribution function of wide applicability, J. Appl. Mech. 18 (1951) 293.

[27] F. Beremin, A. Pineau, F. Mudry, J. Devaux, Y. D'Escatha, P. Ledermann, A local criterion for cleavage fracture of a nuclear pressure vessel steel, Metall. Trans. A 14 (1983) 2277.

[28] M. Miller, K. Powers, R. Nanstad, P. Efsing, Atom probe tomography characterizations of high nickel, low copper surveillance RPV welds irradiated to high fluencies, J. Nucl. Mater. 437 (1–3) (2013) 107.

[29] K. Gott and Y. Haag, "Barsebäck 2, RA 90 Surveillanceprovning av reaktortank-material," Studsvik/NS-90/152 rev 1. 2022

[30] N. Hytönen, Z. Que, P. Arffman, J. Lydman, P. Nevasmaa, U. Ehrnstén, P. Efsing, Effect of weld microstructure on brittle fracture initiation in the thermally-aged boiling water reactor pressure vessel head weld metal, Int. J. Miner. Metall. Mater. 28 (2021) 867–876.

[31] M. Lindroos, J.M. Scherer, S. Forest, A. Laukkanen, T. Andersson, J. Vaara, A. Mäntylä, T. Frondelius, Micromorphic crystal plasticity approach to damage regularization and size effects in martensitic steels, Int. J. Plast. 151 (2022) 103187.

[32] O. Aslan, N. Cordero, A. Gaubert, S. Forest, Micromorphic approach to single crystal plasticity and damage, Int. J. Eng. Sci. 49 (12) (2011) 1311–1325.

[33] P. Sabnis, S. Forest, J. Cormier, Microdamage modelling of crack initiation and propagation in FCC single crystals under complex loading conditions, Comput. Methods Appl. Mech. Eng. 312 (2016) 468–491.

[34] J. Scherer, J. Besson, S. Forest, J. Hure, B. Tanguy, Strain gradient crystal plasticity with evolving length scale: application to voided irradiated materials, Eur. J. Mech. A Solids 77 (2019) 103768.

[35] J. Scherer, J. Besson, S. Forest, J. Hure, B. Tanguy, A strain gradient plasticity model of porous single crystal ductile fracture, J. Mech. Phys. Solids 156 (2021) 104606.

[36] M. Lindroos, T. Andersson, J. Metsäjoki, A. Laukkanen, Crystal Plasticity with micromorphic regularization in assessing scale dependent deformation of polycrystalline doped copper alloys, Crystals 11 (2021) 994.

[37] T. Hoc, S. Forest, Polycrystal modelling of IF-Ti steel under complex loading path, Int. J. Plast. 17 (1) (2001) 65–85.

[38] M. Lindroos, A. Laukkanen, T. Andersson, J. Vaara, A. Mäntylä, T. Frondelius, Micromechanical modeling of short crack nucleation and growth in high cycle fatigue of martensitic microstructures, Comput. Mater. Sci. 170 (2019) 109185.

[39] J. Byun, J. Shim, Y. Cho, D. Lee, Non-metallic inclusion and intragranular nucleation of ferrite in Ti-killed C–Mn steel, Acta Mater. 49 (12) (2003) 593–1606.

[40] J. Shim, Y. Oh, Y. Cho, J. Shim, J. Byun, D. Lee, Ferrite nucleation potency of non-metallic inclusions in medium carbon steels, Acta Mater. 49 (12) (2001) 2115–2122.

[41] S. Babu, H. Bhadeshia, A direct study of grain boundary allotriomorphic ferrite crystallography, Mater. Sci. Eng. A 142 (2) (1991) 209–219.

[42] L. Cheng, X. Wan, K. Wu, Three-dimensional morphology of grain boundary Widmanstätten ferrite in a low carbon low alloy steel, Mater. Charact. 61 (2) (2010) 192–197.

[43] L. Cheng, K. Wu, X. Wan, R. Wei, *In-situ* observation on the growth of Widmanstätten sideplates in an Fe–C–Mn steel, Mater. Charact. 87 (2014) 86–94.

[44] D. Phelan, R. Dippenaar, Widmanstätten ferrite plate formation in low-carbon steels, Metall. Mater. Trans. A 35 (2004) 3701–3706.

[45] D. Phelan, N. Stanford, R. Dippenaar, *In situ* observations of Widmanstätten ferrite formation in a low-carbon steel, Mater. Sci. Eng. A 407 (1–2) (2005) 127–134.

[46] H. Bhadeshia, L. Svensson, Modelling the evolution of microstructure in steel weld metal, in: Mathematical Modelling of Weld Phenomena, Institute of Materials, London, 1993, pp. 109–182.

[47] W. Filho, A. Carvalho, P. Bowen, Micromechanisms of cleavage fracture initiation from inclusions in ferritic welds part I. quantification of local fracture behavior observed in notched testpieces, Mater. Sci. Eng. A 460–461 (2007) 436–452.

[48] J. Lydman, S. Lindqvist, P. Nevasmaa, U. Ehrnstén, "Microstructural characterization of non-irradiated Barsebäck RPV base material and weld metal," VTT Report, VTT-R-05125-18, 2018, Espoo Finland.

[49] Z. Que, H. Seifert, P. Spätig, J. Holzer, A. Zhang, G. Rao, S. Ritter, Environmental degradation of fracture resistance in high-temperature water environments of low-alloy reactor pressure vessel steels with high sulphur or phosphorus contents, Corros. Sci. 154 (2019) 191–207.

[50] M. Boåsen, Modeling of Structural Integrity of Aged Low Alloy Steels Using Non-Local Mechanics, KTH Royal Institute of Technology, Stockholm, Sweden, 2020.